Chapter 4

Investigations on Z-scheme $Ag_3PO_4/CuWO_4$ for antibiotic degradation

4.1. Introduction

Continuous urbanization and industrialization have increased water pollution due to dyes, micropollutants, and heavy metals being discharged into natural water sources (Andreozzi et al., 1999; Cosgrove & Loucks, 2015; Pimentel D et al., 2004; Zyoud et al., 2017). A more recent development is pollution due to antibiotics. This class of pharmaceuticals is poorly absorbed by the treated animal or human and excreted into the environment without being appropriately metabolized (Soltani et al., 2019). The environmental presence of antibiotics increases the resistance of the target bacteria/microorganisms (Daghrir & Drogui, 2013; Manikandan et al., 2022). Approaches such as adsorption, membrane separation, electrolysis, and photocatalysis have been employed to remove antibiotics from natural water (Pei et al., 2021; Xiong & Tang, 2021). Among these alternatives, semiconductor photocatalysis is a reliable, cost-effective, and green approach for the oxidative degradation of such organic pollutants (Deng & Zhao, 2015; H. Wang et al., 2014).

Photocatalysis involves the photo-excitation of electrons in the valence band (VB) to the semiconductor's conduction band (CB). The created holes can oxidize species with more positive reduction potential depending on the VB position. Similarly, the CB position relative to the reduction potential of a molecular species determines the possibility of its photo-reduction. Excited charge carriers form active species like h^+, $O_2^{\bullet-}$, and $^{\bullet}OH$ radicals responsible for organic pollutant degradation (Sarkar et al., 2013). However, a single-component photocatalyst suffers from rapid recombination, inadequate VB/CB positions, and adsorption properties (Jatav et al., 2021). A staggered bandgap heterojunction prevents rapid recombination, enhances charge separation, and improves photocatalytic activity (Asadollahi et al., 2017; Askari et al., 2020).

The species to be reduced or oxidized must adsorb to the relevant heterojunction photocatalyst component. This chapter uses the above strategy to fabricate a new

heterojunction photocatalyst. We first chose $CuWO_4$, a well-known n-type semiconductor with a 2.2-2.4 eV bandgap, as the oxidation component (J. F. Li et al., 2018; Raizada et al., 2020). $CuWO_4$-based heterojunction photocatalysts have exhibited proper water-splitting or organic pollutant photocatalytic degradation properties (Thiruppathi et al., 2019). The second component selected to form a heterojunction photocatalyst with $CuWO_4$ was Ag_3PO_4. The latter is also a visible bandgap semiconductor with a more negative CB position (Luo et al., 2014). Unfortunately, pure Ag_3PO_4 has relatively low chemical stability (Shi et al., 2019). Its photo activity decreases with Ag content due to the formation of Ag layers on the surface of Ag_3PO_4. The Ag layers shield light absorption, inhibiting the transfer of holes from the VB of Ag_3PO_4 to the interface between the photocatalyst and solution. It also hinders the contact of dye molecules with Ag_3PO_4, gradually deteriorating the photocatalytic activity. This deterioration of the Ag_3PO_4 photocatalytic activity limits its practical application as a recyclable photocatalyst. Coupling Ag_3PO_4 with another semiconductor can form a heterojunction photocatalyst with enhanced photocatalytic efficiency (L. Xu et al., 2014). Heterojunction photocatalysts have improved photoexcited charge separation and lifetimes (Huang et al., 2019).

Hence, this chapter investigates the photocatalytic properties of the heterojunction $Ag_3PO_4/CuWO_4$ photocatalyst for CIP degradation. The $Ag_3PO_4/CuWO_4$ composite is prepared by a stepwise precipitation hydrothermal method. Niu et al. (Earth and Environmental Science 2019, Vol. 344, No. 1, p. 012069, IOP Publishing) have reported the synthesis of Ag_3PO_4 through different methods. These include the solid phase, hydrothermal, and direct precipitation methods. They found that the sample synthesis by the hydrothermal method resulted in more uniformly sized Ag_3PO_4 particles. Thus, hydrothermal condition is critical in the synthesis of Ag_3PO_4

nanocomposite. Considering these facts, Ag_3PO_4 has been prepared by the hydrothermal method in this thesis.

Besides CIP, the photocatalytic activity of the $Ag_3PO_4/CuWO_4$ composite was also evaluated for tetracycline (TET) degradation. The latter is another frequently used antibiotic for human and veterinary practices. The photocatalytic activity varied with the extent of Ag_3PO_4 loading on $CuWO_4$, with an intermediate deposition of the former exhibiting the best activity. The photocatalytic activities of these heterojunction photocatalysts were compared with pure $CuWO_4$ and Ag_3PO_4 materials. Materials prepared were characterized by powder X-ray diffraction (XRD), transmission electron microscopy (TEM), and X-ray photoelectron spectroscopy (XPS). The relative recombination of photoinduced charge carriers was analysed by photoluminescence spectroscopy. The reactive species trapping experiment results led to the CIP photocatalytic degradation mechanism.

4.2. Experimental

4.2.1. Hydrothermal synthesis of $Ag_3PO_4/CuWO_4$

Under constant stirring, one mmol of $CuWO_4$ nanoparticles was re-dispersed in 60 ml DI water. Afterward, an $AgNO_3$ solution (1 mmol in 20 ml DI water) was mixed with the $CuWO_4$ dispersion. This mixture was then agitated for 24 hours for proper adsorption of Ag^+ ions on the surface of $CuWO_4$ nanostructures. Next, 20 ml of Na_2HPO_4 solution was added dropwise at constant stirring to the above-prepared reaction mixture. The total mixture was then transferred to a 100 ml Teflon autoclave and kept at 120 ^{0}C for 24 hours. The precipitate obtained was washed with DI water several times and finally washed with ethanol. After washing, the precipitate was dried in a vacuum at 60 ^{0}C for 24 hours. The final product had a 10% weight percent of Ag_3PO_4 loaded on the $CuWO_4$ nanoparticles. The 10%AW abbreviation hereafter represents this composite. Two more $Ag_3PO_4/CuWO_4$ composites were prepared with

20 and 30 weight percent of Ag_3PO_4 (per weight unit of $CuWO_4$). These are abbreviated by 20%AW and 30%AW symbols in the rest of this chapter (Scheme 4.1).

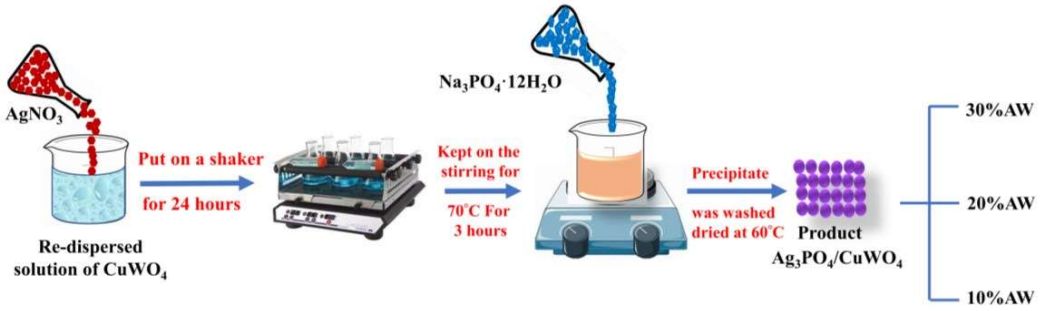

Scheme 4.1: Graphical representation of $Ag_3PO_4/CuWO_4$ composite nanoparticle synthesis

4.2.2. Photocatalytic activity of $Ag_3PO_4/CuWO_4$

The photocatalytic properties of $Ag_3PO_4/CuWO_4$ composites were evaluated for TET and CIP degradation under visible light irradiation. The light source was a cool white LED with 1070 W/m^2 intensity. The reaction was carried out in a 1cm path-length cuvette. Two separate 20 ppm solutions of CIP and TET at pH (performed the experiments at different pH, and optimum pH was 3) three were prepared, and 200ul each of the photocatalyst (2mg/4ml) dispersion was added to the respective organic pollutant solution. The mixtures prepared were stirred in the dark for 1 hour to enable adsorption-desorption equilibrium. In this process ~5-8% of CIP/TET is adsorbed on catalyst surface. After that, each reaction mixture was put under the visible light source. The degradation of the targeted organic pollutant molecules was monitored by UV visible spectrophotometry at periodic time intervals.

$$\text{Removal Efficiency} = \left(\frac{C_o - C_t}{C_o}\right)x100 \qquad \ldots. (4.1)$$

In equation (4.1), the notation C_0 represents the initial concentration, and C_t is the final concentration.

4.3. Result and Discussions

4.3.1. XRD Analysis

Fig. 4.1 displays the XRD patterns of the $CuWO_4$, Ag_3PO_4, and their composites. The XRD of pure $CuWO_4$ has intense peaks at 2θ values 19°, 22.9°, 23.5°, 24.1°, 25.9°, 26.9°, 28.7°, 30.8°, 31.6°, 32.1°, 34.4°, and 38.6°. These could be indexed to the $CuWO_4$ triclinic structure (JCPDS File No. 72-0616) crystal planes (001), (100), (110), (0 $\bar{1}$1), (0 $\bar{1}$ $\bar{1}$), (011), ($\bar{1}$01), (101), ($\bar{1}$01), ($\bar{1}$ $\bar{1}$ 1), (111), (020), ($\bar{1}$11), (1$\bar{1}$1), (111), (020), ($\bar{1}$11), (1 $\bar{1}$1), (120), and (200), respectively (K. Li et al., 2019). The prepared Ag_3PO_4 XRD pattern was indexed to its body-centered cubic structure (JCPDS File No. 06- 0505). The XRD d-spacings at (2θ) 20.1°, 32°, 36.7° and 55.1° matched with those of (100),(110), (221) and (111) planes respectively (You et al., 2019). XRD patterns of the 10% AW, 20% AW, and 30% AW composites have peaks corresponding to $CuWO_4$ and Ag_3PO_4.

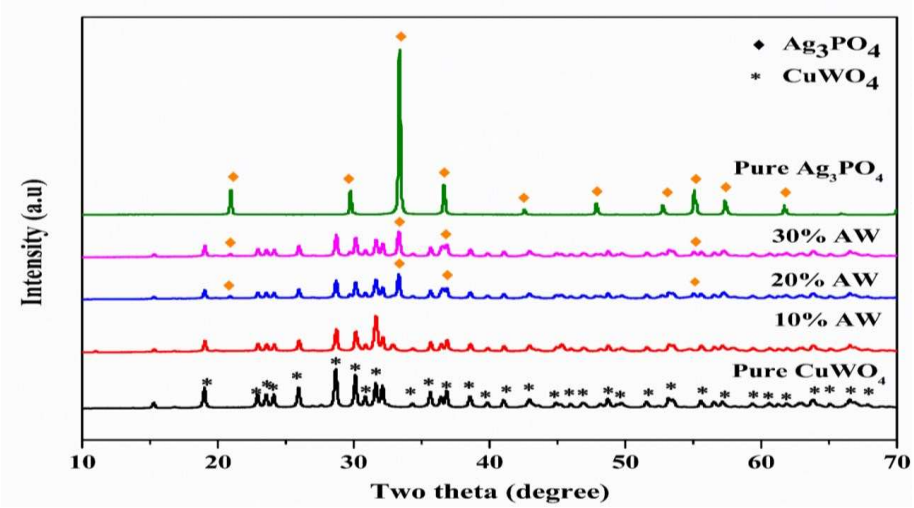

Fig. 4.1: XRD patterns of as-prepared $CuWO_4$, Ag_3PO_4, 10% AW, 20% AW, and 30% AW

4.3.2. FTIR Analysis

Figure 4.2 displays the FTIR spectrum of the composite. It has been compared with the FTIRs of pure Ag_3PO_4 and $CuWO_4$ samples (from the literature) to understand the

interactions between these components of the composite. The asymmetric stretching of the P-O-P group occurs at 1087 cm^{-1} in the FTIR of Ag_3PO_4 only. This band red-shifts to 1045 cm^{-1} in the composite FTIR. Lastly, the P-O-P symmetric stretching vibration displays a peak of 864 cm^{-1} in the Ag_3PO_4 FTIR. This particular peak blue shifts to 912 cm^{-1} in the composite FTIR. Compared to these, the stretching mode of W=O (in the WO_4^{2-} part of $CuWO_4$) at 950 cm^{-1} blue shifts to 994 cm^{-1} in the composite FTIR. Overall, due to composite formation, there are changes in the different FTIR vibration modes associated with the P-O bonds and in the W=O stretching mode. This suggests that Ag_3PO_4 and $CuWO_4$ components interact through some association between the $P\text{-}O^-$ and W=O units. However, the composite formation does not cause any change in the 580 cm^{-1} Cu-O stretching vibrations (Balasubramanian et al., 2020), indicating that this part is not involved in composite formation.

Note that the composite also displays FTIR peaks at 3421 cm^{-1} and 1640 cm^{-1}, corresponding to the O-H stretching and H-O-H bending modes. Furthermore, the sharp peak at 1385 cm^{-1} corresponds to nitrate impurities due to some unreacted $AgNO_3$ precursor (Ma et al., 2022).

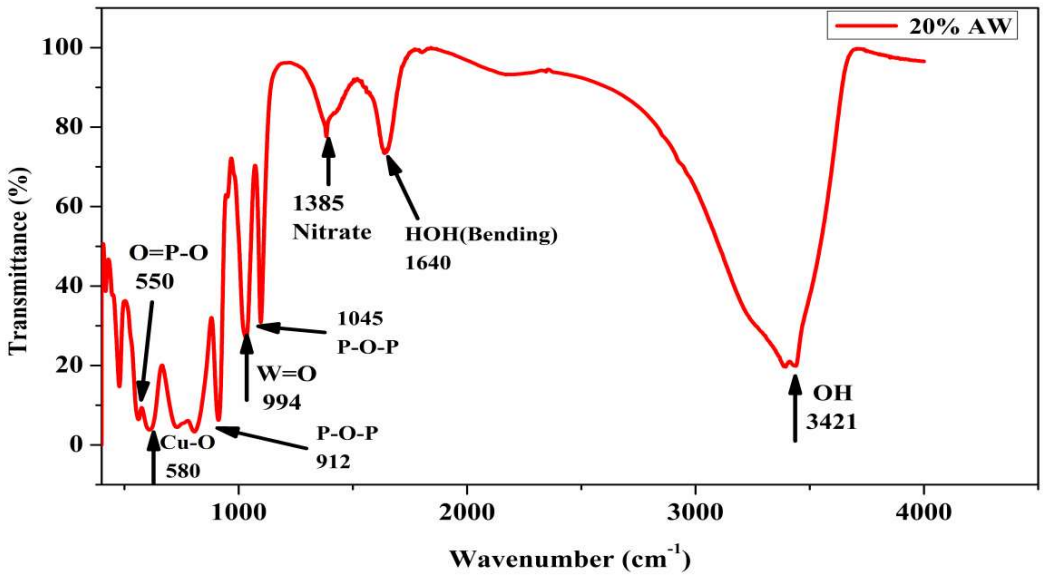

Fig. 4.2: FT-IR spectrum of 20% AW photocatalyst

4.3.3. Morphology and heterostructures interface analysis

Fig. 4.3a-d show the TEM images of pure $CuWO_4$, 10% AW, and 30% AW. As-prepared $CuWO_4$ nanostructures (Fig. 4.3) have pentagonal and hexagonal structures. The fringes in the HRTEM image of pure $CuWO_4$ could be indexed to the (110) plane (Fig. 4.4b)

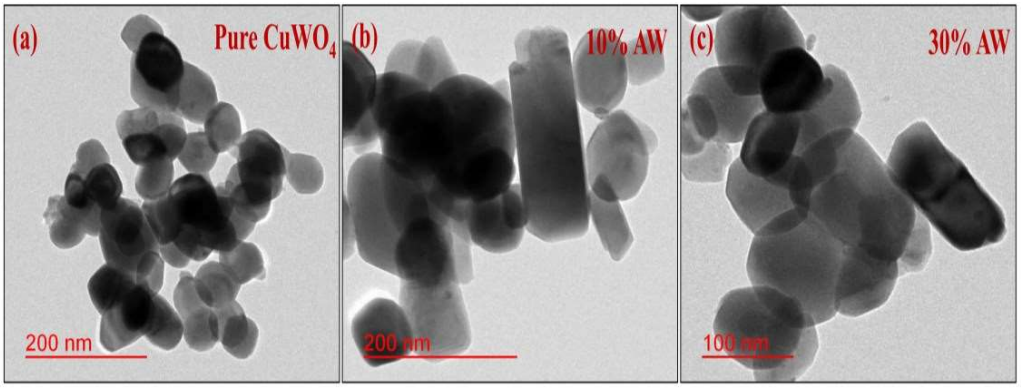

Fig. 4.3: TEM images of (a) Pure $CuWO_4$, (b) 10% AW, and (c) 30% AW

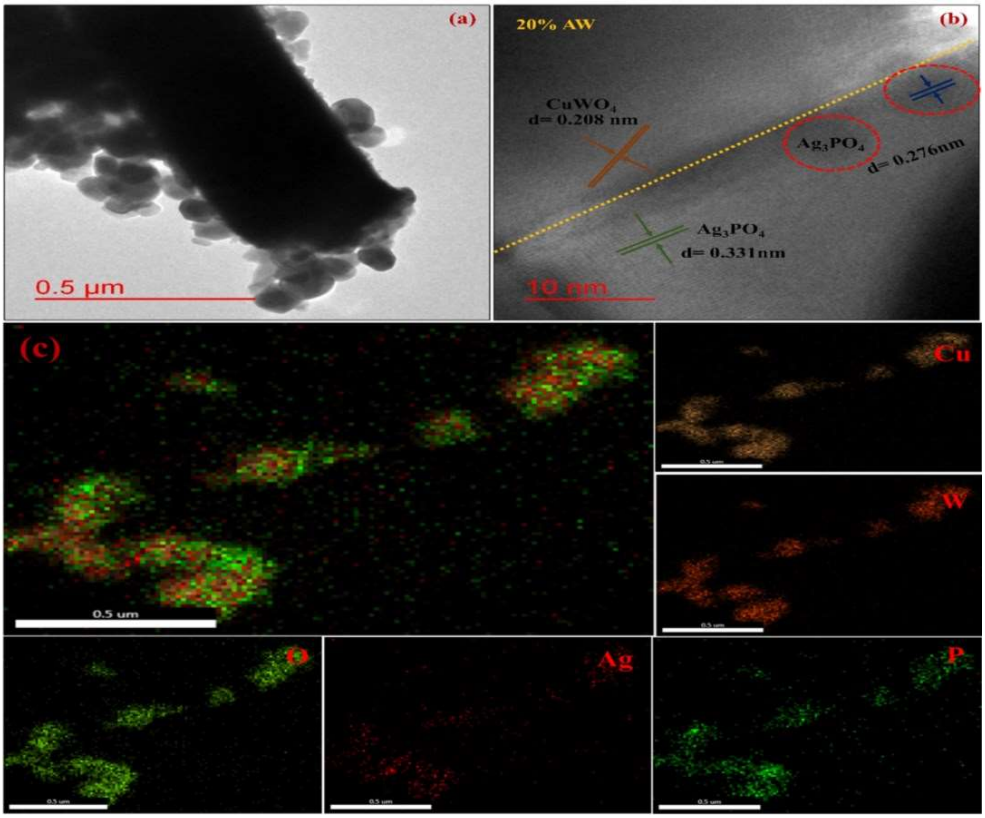

Fig. 4.4: (a) TEM, (b) HR-TEM, and (c) elemental mapping images of the 20% AW photocatalyst

Fig. 4.4 displays the TEM, HR-TEM, and elemental mapping images of the 20%AW sample since it has better photocatalytic activity than other materials in this study. Approximately spherical $CuWO_4$ nanostructures are in close contact with an Ag_3PO_4 rod (Fig. 4.4a). This interpretation is confirmed by the HR-TEM (Fig. 4.4b) and elemental mapping images (Fig. 4.4c). The HRTEM image (Fig. 4.4b) of 20%AW has two fringes with lattice spacings 0.208 and 0.331 nm. These could be indexed to the $CuWO_4$ (110) and the Ag_3PO_4 (220) planes, respectively. Adjacent $CuWO_4$ and Ag_3PO_4 phases make photoinduced charge carrier separation possible, giving higher photocatalytic efficiency.

4.3.4. XPS analysis

The survey and the high-resolution (HR) XPS spectrums of $CuWO_4$, Ag_3PO_4, and 20% AW were analysed. The peaks of Cu, W, O, Ag, and P in the survey spectrum of 20% AW (Fig. 4.5) confirm the presence of these elements in it. The binding energies (BE) in the spectra of different samples were calibrated to the C1s peak of 284.8 eV. Fig. 4.6 compares the HR spectrums of elements in $CuWO_4$ and Ag_3PO_4 with the same species in 20% AW. The Cu2p region HR spectrum (Fig. 4.6a) of $CuWO_4$ exhibits $Cu2p_{3/2}$, and $Cu2p_{1/2}$ peaks at 934.2 eV and 954.1 eV, respectively. The corresponding peaks in the 20% AW XPS shift to 934.5 and 954.3 eV, respectively. Similarly, the W4f (+6 oxidation state of W) region Fig. 4.6b also has two peaks at 35.1 and 37.3 eV ($W4f_{3/2}$ and $W4f_{½}$, respectively). These peaks appear at 35.5 and 37.7 eV in the 20% AW spectrum. However, the composite's two Ag3d peaks (Fig. 4.6d) are at slightly lower BEs than the pure Ag_3PO_4 plot. The P_{2p} spectrum (Fig. 4.6e) of pure Ag_3PO_4 at 132.4 eV corresponds to the +5 oxidation state of phosphorus. The same peak in the 20% AW spectrum undergoes a negative shift to 132 eV.

The deconvoluted O1s peaks of $CuWO_4$ are at 530.3 and 531.9 eV, respectively (Fig. 4.6c). Then pure Ag_3PO_4 XPS peaks are at 529.9 eV and 531.6 eV. In the 20%

AW spectrum, these peaks appear at 530.3 eV, 531.3 eV, and 532.4 eV, respectively. Since oxygen is present in the composite's $CuWO_4$ and Ag_3PO_4 parts, one cannot ascribe the observed shift to any component. Overall, Cu and W binding energies in 20% AW have higher values than those observed in the pure $CuWO_4$ spectrum. The BEs of Ag and P in the 20% AW spectrum show slightly lesser values than those observed for pure Ag_3PO_4. Electron transfer from $CuWO_4$ to Ag_3PO_4 causes a positive BE shift in the $CuWO_4$ part and a negative BE shift in the Ag_3PO_4 component (Q. Xu et al., 2018). Photo-excitation, therefore, results in the migration of electrons from $CuWO_4$ to Ag_3PO_4.

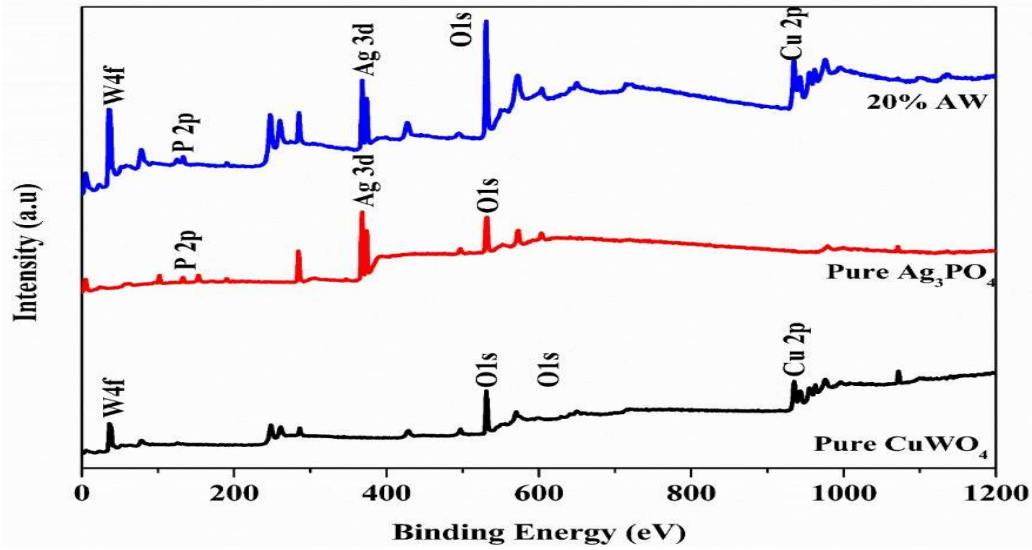

Fig. 4.5: Survey peak of as-prepared samples pure $CuWO_4$, 20% AW, and pure Ag_3PO_4 samples

Fig. 4.7(a) and 4.7(b) display the valence band XPS spectra of $CuWO_4$ and Ag_3PO_4. The VB maximum position was located from the intersection of the fits to the two linear portions of this curve (L. Wang et al., 2016). VB positions of $CuWO_4$ and Ag_3PO_4 are 1.66 eV and 1.04 eV, respectively.

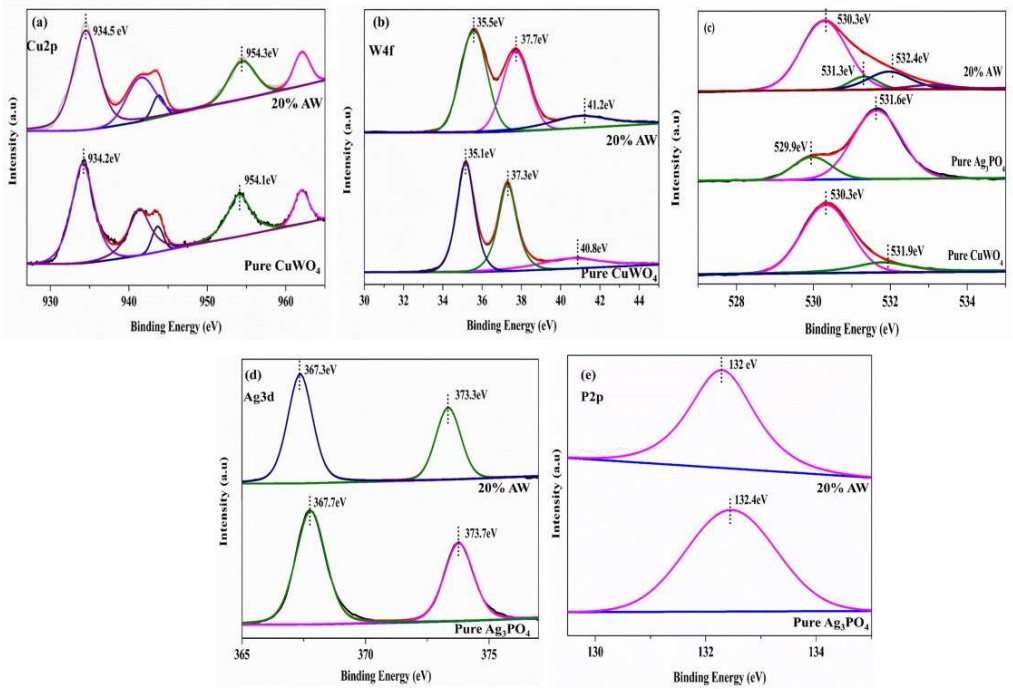

Fig. 4.6: Comparison between HR-XPS spectrums of different regions of 20% AW with the spectrums of Ag_3PO_4 and $CuWO_4$ (a) Cu2p (b) W1s (c) O 1s (d) Ag 2p (e) P 2p and the valence band spectra of $CuWO_4$ (f) and Ag_3PO_4 (g)

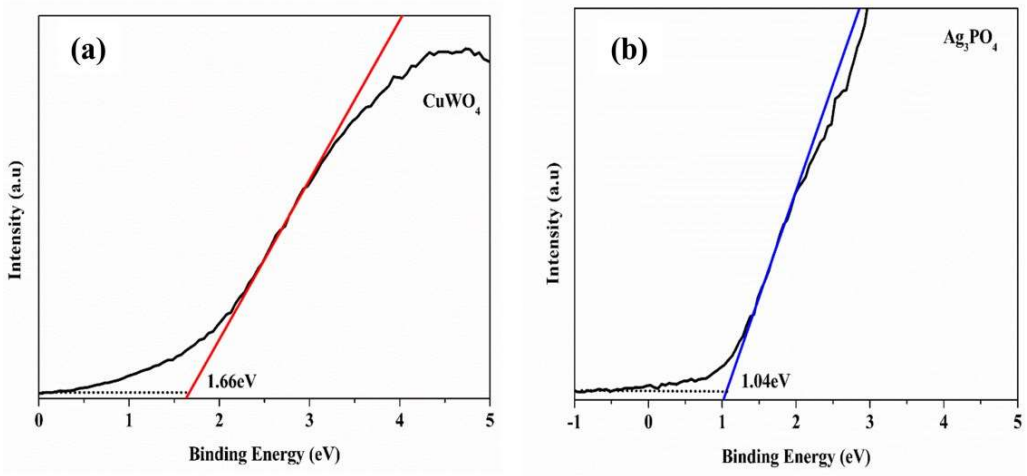

Fig. 4.7: the valence band spectra of (f) $CuWO_4$ and (g) Ag_3PO_4

4.3.5. Bandgap studies through UV-visible Spectroscopy

Fig. 4.8(a) shows the solid-state UV-visible absorption spectra of the prepared catalysts. The absorption edge of the composite samples is almost in the same visible

wavelength range. Fig. 4.8(b) and 4.8(c) display the Tauc plots of pure $CuWO_4$ and Ag_3PO_4 phases. The Tauc relation (Eq. 4.2) was used to make the plot.

$$(\alpha h\upsilon)^{1/n} = h\upsilon - E_g \qquad (4.2)$$

In equation (4.2), α is the molar absorptivity coefficient, h denotes Planck's constant, υ is the frequency, and Eg is the bandgap energy. The exponent value of n is 2 for direct transition and 1/2 for indirect transition. The x-axis intercept of the fit to the linear portion of the Tauc plots gave the bandgaps of these phases (De et al., 2020; Liu et al., 2019). The indirect bandgaps of the pure $CuWO_4$ and Ag_3PO_4 are 2.2 eV and 2.4 eV, respectively. Furthermore, Eq. 4.3 determined the CB positions of $CuWO_4$ and Ag_3PO_4 (Walsh & Butler, 2014).

$$E_{CB} = E_{VB} - Eg \qquad (4.3)$$

The calculated CB positions of $CuWO_4$ and Ag_3PO_4 are -0.54 and -1.36 eV.

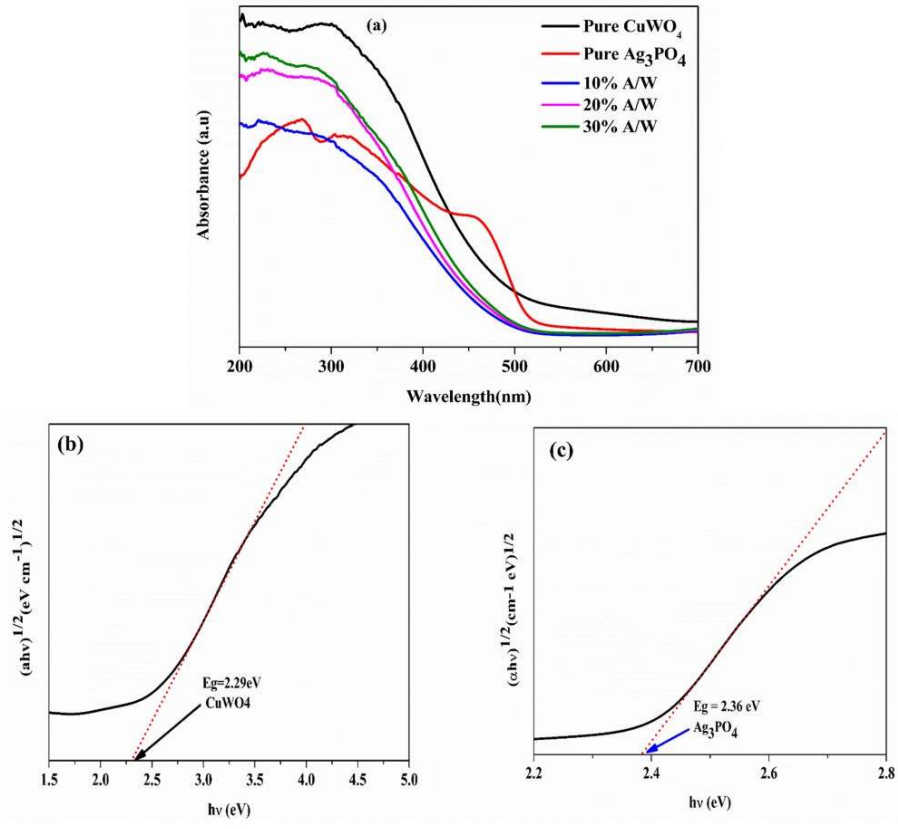

Fig. 4.8: (a) Solid-state UV-Vis diffuse absorbance spectra of different samples (b) Tauc plot of pure $CuWO_4$ (c) Tauc plot of pure Ag_3PO_4

4.3.6. Photoluminescence analysis

Photoluminescence analysis of the samples revealed their relative photo-excited electron-hole recombination efficiency (Jatav et al., 2021). The excitation wavelength of the composites was 269 nm. Fig. 4.9 shows the photoluminescence spectra of the composite samples with different loading of Ag_3PO_4 on the surface of $CuWO_4$. The precipitation of Ag_3PO_4 on $CuWO_4$ decreases the fluorescence peak intensity. Thus, the interfacial contact between Ag_3PO_4 and $CuWO_4$ enhances charge separation and decreases the recombination rate of photoinduced charge carriers. The fluorescence spectrum of the 20% AW sample exhibits the lowest intensity, indicating that this is the optimum $Ag_3PO_4/CuWO_4$ composition. Excessive loading of Ag_3PO_4 blocks the photo-excitation of the $CuWO_4$ surface.

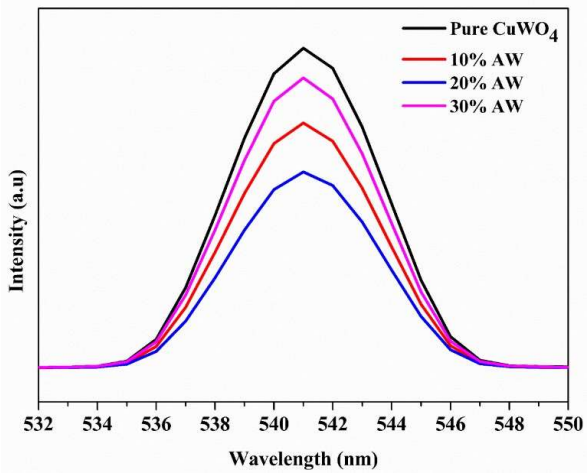

Fig. 4.9: Photoluminescence of the as-prepared samples Pure $CuWO_4$, 10% AW, 20% AW, and 30% AW

4.3.7. Evaluation of the photocatalytic activity

The photocatalytic activities of as-prepared samples were tested for the visible light degradation of TET and CIP. These antibiotics did not degrade under visible light without any photocatalyst. Visible light degradation of CIP and TET was attempted over all samples prepared in this study. Fig. 4.10 shows the degradation plots of CIP and TET degradation over the investigated photocatalysts. CIP and TET degradation

on $CuWO_4$ nanoparticles is negligible. Though slow, some CIP and TET degradation over Ag_3PO_4 nanostructures occurs. Compared to this, there is a slight increase in the CIP and TET degradation rate over 10%AW. CIP and TET photocatalytic degradation are better than the 30%AW and 20%AW samples. The 20% AW sample exhibits the best photocatalytic activity for CIP and TET degradation. Depositing Ag_3PO_4 on $CuWO_4$ causes charge separation and better reduction/oxidation driving forces. But it also blocks the light from falling on $CuWO_4$. Hence, the photocatalytic activity of the composite is a result of these competing factors. Figure 4.10b shows that the TET absorption peak at 357 nm goes down with time but the peak at 260 nm shows negligible change with time.

Fig. 4.11 shows that CIP and TET degradation on nanomaterials prepared in this study followed zero-order kinetics. The turnover frequencies (TOF) have also been calculated because the degradation kinetics order can change with the photocatalyst.

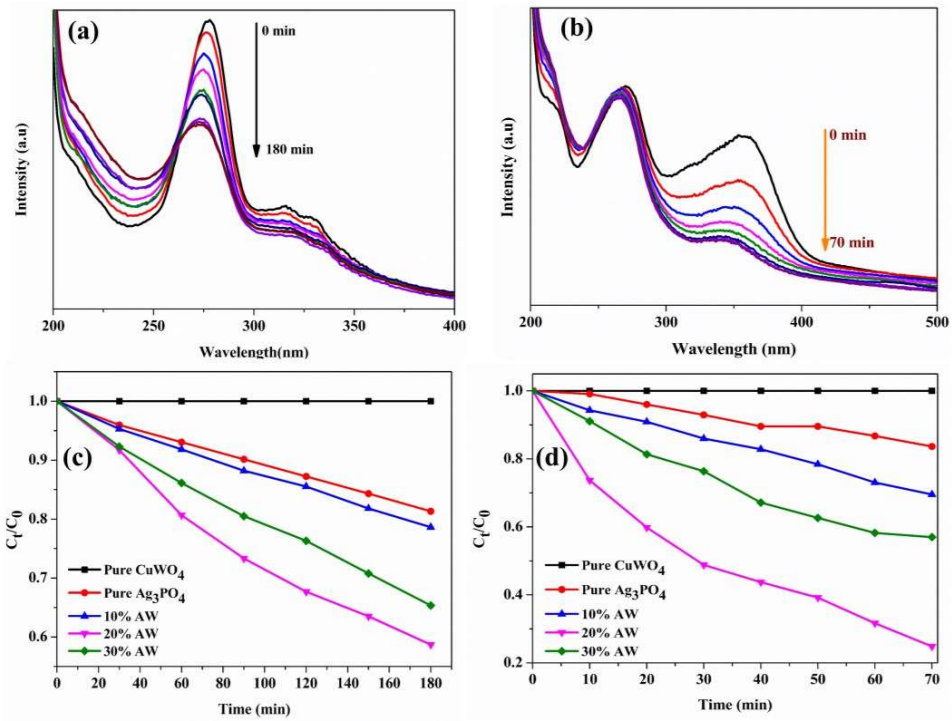

Fig. 4.10: UV-visible spectra of CIP (a) and TET (b) versus time in the presence of catalyst 20% AW, and change in normalized (c) CIP concentration and (d) TET

concentration with visible light exposure over pure $CuWO_4$, Ag_3PO_4, 10% AW, 20% AW, and 30% AW, respectively.

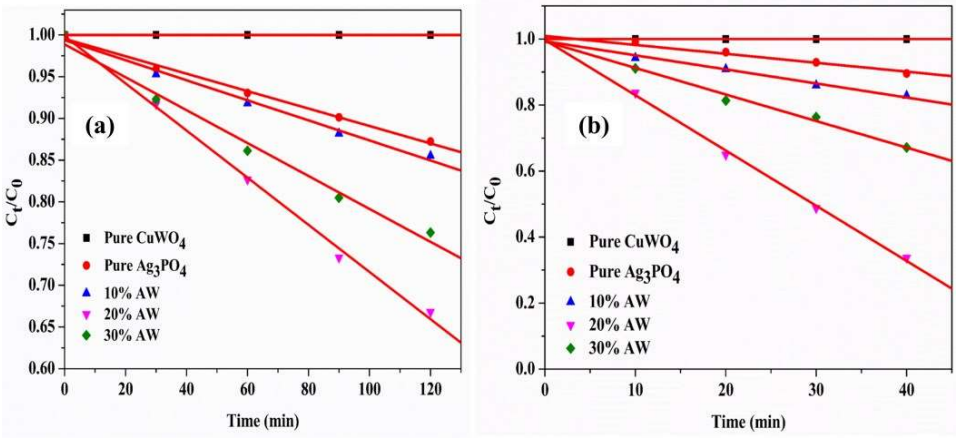

Fig. 4.11: Zero-order kinetics for (a) CIP and (b) TET degradation on the pure $CuWO_4$, Ag_3PO_4, 10% AW, 20% AW and 30% AW nanocomposites

The details of RhB and CIP degradation kinetics are given in Tables 4.1 and 4.2.

Table 4.1: Rate constant (k) and correlation coefficient (R^2) for TET degradation on pure $CuWO_4$, Ag_3PO_4, 10% AW, 20% AW, and 30% AW photocatalysts.

Catalysts	Rate constant (mol L^{-1} sec^{-1})	R^2
Pure $CuWO_4$	1×10^{-4}	0.999
Pure Ag_3PO_4	4.4×10^{-3}	0.989
10% AW	6.5×10^{-3}	0.993
20% AW	2.7×10^{-2}	0.985
30% AW	9.4×10^{-3}	0.975

Table 4.2: Rate constant (k) and correlation coefficient (R^2) of CIP degradation on pure $CuWO_4$, Ag_3PO_4, 10% AW, 20% AW, and 30% AW photocatalysts.

Catalysts	Rate constant (mol $L^{-1}sec^{-1}$)	R^2
Pure $CuWO_4$	1.2×10^{-3}	0.999
Pure Ag_3PO_4	3.2×10^{-3}	0.993
10% AW	4.6×10^{-3}	0.998
20% AW	6.5×10^{-3}	0.996
30% AW	2.4×10^{-3}	0.984

Table 4.3 and 4.4 compares the TOF over different photocatalysts from articles published previously in the literature. The TOF value exhibited over 20%AW is among the best values reported in the literature for CIP degradation.

Table 4.3: Comparison of CIP degradation turnover frequency (TOF) values over different photocatalysts with 20% AW.

Photocatalysts	Light source	Turnover frequency ($mol.g^{-1}.min^{-1}$)	References
Ag_3PO_4/WO_3	300W Xe lamp	3.3×10^{-3}	(T. Wang et al., 2016)
$Ag_3PO_4/BiPO_4$	500W Xe lamp	1×10^{-3}	(Zhu et al., 2022)
$AgI/CuWO_4$	Cool white LED (1070 W/m^2)	0.5×10^{-3}	(Jatav et al., 2021)
$Ag_3PO_4/CuWO_4$	Cool white LED (1070 W/m^2)	1.6×10^{-3}	This Work

Table 4.4: Comparison of TET degradation turnover frequency (TOF) values over different photocatalysts with 20% AW.

Photocatalysts	Light source	Turnover frequency ($mol.g^{-1}.min^{-1}$)	References
AgI/WO_3	300W Xe lamp	0.12×10^{-3}	(T. Wang et al., 2016)
Ag_3PO_4/WO_3	500W Xe lamp	1.5×10^{-3}	(You et al., 2019)
$Ag_3PO_4/CoWO_4$	300W Xe lamp	5.1×10^{-3}	(L. Xu et al., 2022)
$Ag_3PO_4/CuWO_4$	Cool white LED (1070 W/m^2)	2.3×10^{-3}	This Work

4.3.8. Recyclability

The recyclability of the 20% AW photocatalyst for CIP and TET degradation was tested under visible light irradiation. All cycles had the same experimental conditions. Fig. 4.12(a) displays the reusability of CIP over five cycles in histogram format. Each cycle subjected a fixed concentration of aqueous organic pollutant solution to one-hour visible light photocatalytic conditions. The photocatalyst was recovered and reused in the next cycle under the same conditions. The degradation reported in subsequent cycles was relative to that obtained in the first cycle. By the 5th

cycle, the degradation rate had decreased to 90% of the 1st cycle output. Thus, the photostability of 20%AW is much better than that reported for pure Ag_3PO_4 (H. Wang et al., 2019). Fig. 4.13 gives the XRD of the recycled 20%AW photocatalyst. No change in the phases formed confirmed the stability of the 20% AW sample. The decrease in photocatalytic efficiency could be due to Ag leaching during the reuse of the photocatalyst (Jatav et al., 2021).

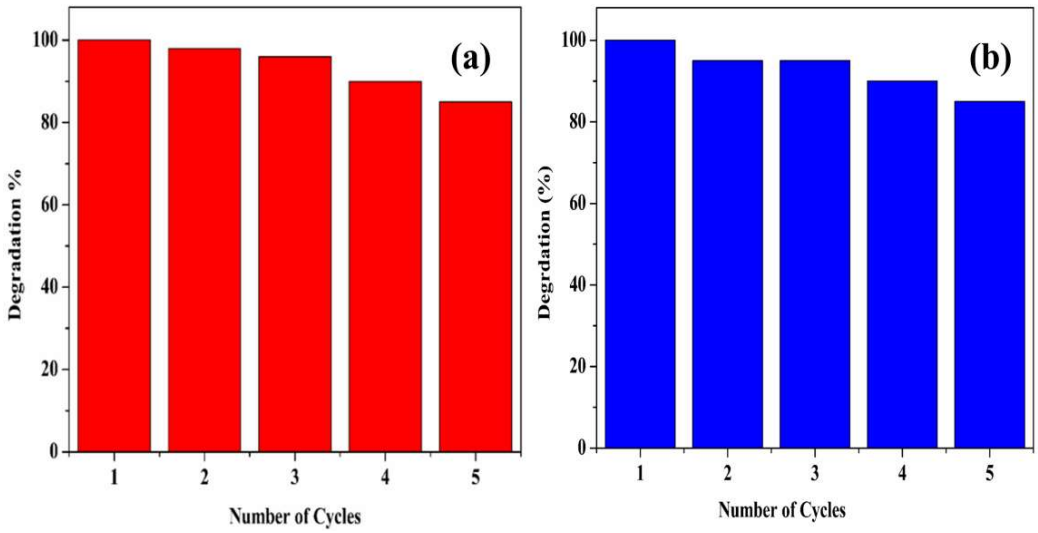

Fig. 4.12: Photocatalytic activity of 20% AW during five cycles of reuse under visible light irradiation for (a) CIP and (b) TET degradation

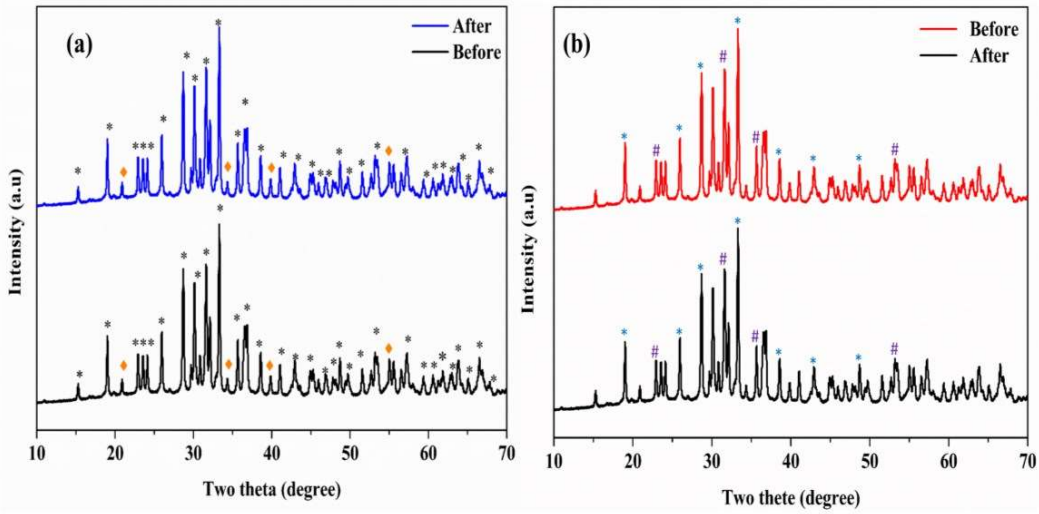

Fig. 4.13: XRD before and after (a) CIP and (b) TET degradation

4.3.9. Active species trapping experiments

Fig. 4.14 gives a bar plot of the variation in CIP and TET degradation when the reaction mixture also had scavengers for specific active species. The first bar denoted in the plot as 'blank' represents the photocatalytic degradation observed in a particular time interval without any scavenger molecule. The subsequent (scavenger) bars are relative to the blank output. Separate photocatalytic experiments were conducted with the reaction mixtures containing equal concentrations of KI, isopropyl alcohol, and p-benzoquinone. Both CIP and TET degradations were most affected by the hole scavenger KI. The superoxide scavenger PBQ also decreased the CIP and TET degradation activity significantly but less than that observed with KI (Vinesh et al., 2022). The hydroxyl radical trapping agent IPA had minimal effect on photocatalytic degradation activity. Thus, the photocatalytic degradation of CIP and TET was mainly by the superoxide pathway.

The last photocatalysis control experiment replaced the solvent (water) with acetonitrile under continuous oxygen purging. The rest of the photocatalysis conditions remained the same. Negligible degradation of CIP and TET was observed under these conditions.

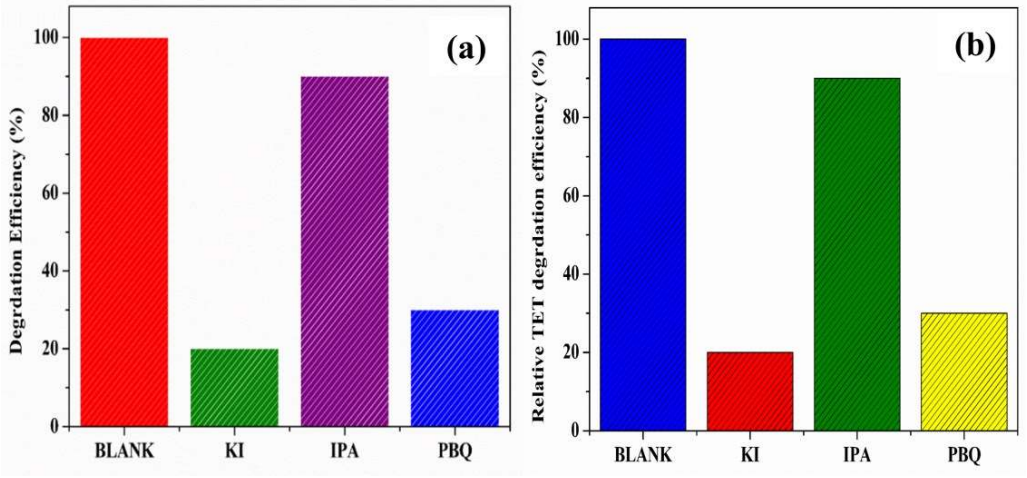

Fig. 4.14: Scavenging experiment histogram plot for determination of the active species during photocatalytic (a) CIP and (b) TET degradation

4.3.10. Photocatalytic reaction mechanism

This section proposes a photocatalytic mechanism based on the investigation results presented earlier. Both components of 20% AW have visible range bandgaps and therefore get photo-excited on irradiation. The XPS analysis points to electron transfer from the $CuWO_4$ side to the Ag_3PO_4 part, following a Z-scheme mechanism. The scavenger experiments conclude that holes and superoxide species drive the photocatalytic reaction. The following Z-scheme mechanism (Fig. 4.15) is proposed based on this collection of results. The photo-excited electrons from the $CuWO_4$ migrate to Ag_3PO_4, while the holes are concentrated on the $CuWO_4$ VB. The holes now get quenched by CIP and H_2O oxidation (Jatav et al., 2021). The latter also produces oxygen which takes part in the reaction on the Ag_3PO_4 side. At the same time, photo-excited electrons on Ag_3PO_4 reduce oxygen molecules to generate the superoxide species. These superoxide radicals again generate various free radical oxidants that oxidize CIP molecules. The superior affinity of both oxygen and CIP towards the Ag_3PO_4 surface aids this phenomenon.

Note the TET peak at 260 nm peak corresponds to the aromatic ring D (refer to Chapter 1). The latter is considerably stable and does not degrade easily. The photocatalytic mechanism suggests that TC oxidation by the present $Ag_3PO_4/CuWO_4$ is due to superoxide radicals and photo-excited holes. Previous literature shows this aromatic ring can only be broken by stronger oxidants like ·OH radicals (Ma et.al, 2022). Since there was no ·OH radical formation during the present photocatalytic process, the 260 nm peak could be degraded.

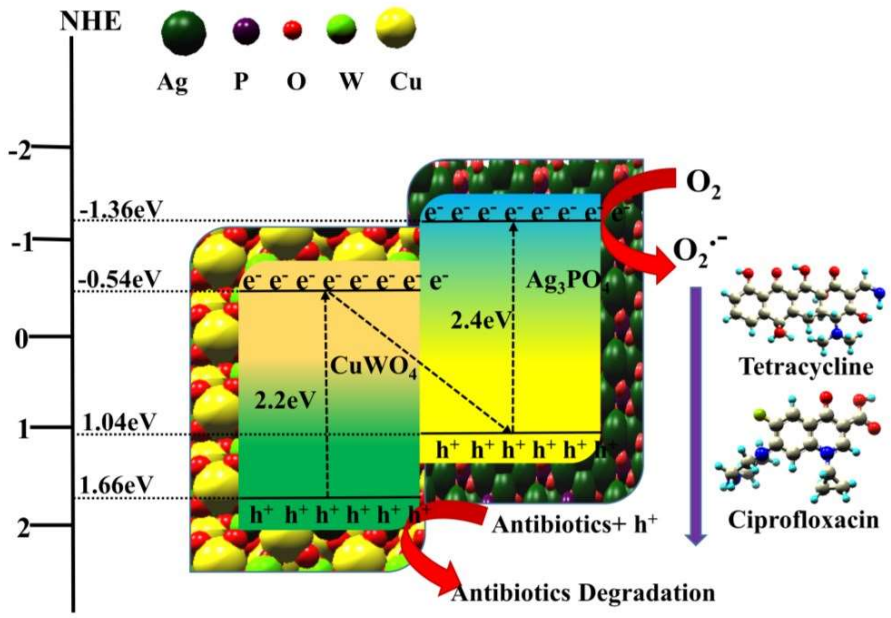

Fig. 4.15: A schematic of the possible photocatalytic mechanism for antibiotic degradation on 20% AW

4.4. Conclusions

Three $Ag_3PO_4/CuWO_4$ nanocomposites were prepared by precipitation of different amounts (10, 20, and 30 weight percent) of Ag_3PO_4 on $CuWO_4$ nanoparticles. The nanocomposite with 20 wt% Ag_3PO_4 loading demonstrated the best photocatalytic efficiency towards ciprofloxacin and tetracycline degradation. Both photocatalytic degradations followed zero-order kinetics. XPS analysis of the binding energies of different elements in the composite showed electron transfer from the $CuWO_4$ to the Ag_3PO_4 side. Photocatalysis experiments with scavenger molecules specific to different reactive species showed that CIP and TET oxidation on photo-excited holes has been rate-limiting. Thus, visible light irradiation photo-excited $CuWO_4$ and Ag_3PO_4 parts, with holes becoming concentrated on $CuWO_4$ and the electrons on the Ag_3PO_4 side. CIP and water oxidation quenched the $CuWO_4$ photoexcited holes, while electrons on Ag_3PO_4 exhibited oxygen reduction to superoxide. The latter, in turn, contributed to CIP and TET oxidation.